Conservation of locomotion-induced oculomotor activity through evolution in mammals

Filipa França de Barros, Julien Bacqué-Cazenave, Coralie Taillebuis, Gilles Courtand, Marin Manuel, Hélène Bras, Michele Tagliabue, Denis Combes, François M Lambert, Mathieu Beraneck

Filipa França de Barros, Julien Bacqué-Cazenave, Coralie Taillebuis, Gilles Courtand, Marin Manuel, et al.. Conservation of locomotion-induced oculomotor activity through evolution in mammals. Current Biology - CB, 2022, 32, pp.453 - 461.e4. 10.1016/j.cub.2021.11.022 . hal-03764860

HAL Id: hal-03764860
https://hal.science/hal-03764860v1

Submitted on 30 Aug 2022

Original article can be found at: https://doi.org/10.1016/j.cub.2021.11.022
Citation: França de Barros et al., 2022, Current Biology 32, 453–461 ; January 24, 2022 © 2021 Elsevier Inc.

Conservation of locomotion-induced oculomotor activity through evolution in mammals

Filipa França de Barros[1], *Julien Bacqué-Cazenave*[2], *Coralie Taillebuis*[1,2], *Gilles Courtand*[2], *Marin Manuel*[3,4], *Hélène Bras*[5], *Michele Tagliabue*[1], *Denis Combes* [2], *François M Lambert* [2, 6,*] , *Mathieu Beraneck* [1, 6, 7, *]

1-Université de Paris, CNRS UMR 8002, INCC - Integrative Neuroscience and Cognition Center, F-75006, Paris, France.

2-Institut des Neurosciences Cognitives et Intégratives d'Aquitaine, INCIA CNRS UMR 5287, 33076 Université de Bordeaux, Bordeaux, France

3-Université de Paris, CNRS UMR 8003, SPPIN - Saints-Pères Paris Institute for the Neurosciences, F-75006 Paris, France.

4-Department of Biomedical and Pharmaceutical Sciences and George and Anne Ryan Institute for Neuroscience, University of Rhode Island, Kingston, RI

5-Institut de Neurosciences de la Timone, UMR 7289 CNRS-AMU, 13385 Marseille, France.

6- Equal contribution

7- Lead contact

*** Corresponding authors**

Dr. M. Beraneck. CNRS UMR 8002, Université de Paris, 45 rue des St-Pères, Paris 75270, France. Email: mathieu.beraneck@u-paris.fr

Dr. FM Lambert CNRS UMR 5287, Université de Bordeaux, 146 rue Léo Saignat, Bordeaux 33076, France. Email: francois.lambert@u-bordeaux.fr

Citation: França de Barros et al., 2022, Current Biology 32, 453–461 ; January 24, 2022 © 2021 Elsevier Inc.

Summary

Efference copies are neural replicas of motor outputs used to anticipate the sensory consequences of a self-generated motor action or to coordinate neural networks involved in distinct motor behaviors[1]. An established example of this motor-to-motor coupling is the efference copy of the propulsive motor command, that supplements classical visuo-vestibular reflexes to ensure gaze stabilization during amphibian larval locomotion[2]. Such feedforward replica of spinal pattern-generating circuits, produces a spino-extraocular motor coupled activity that evokes eye movements, spatio-temporally coordinated to tail undulation independently of any sensory signal[3,4]. Exploiting the developmental stages of the frog[1], studies in metamorphing Xenopus demonstrated the persistence of this spino-extraocular motor command in adults, and its developmental adaptation to tetrapodal locomotion[5,6]. Here, we demonstrate for the first time the existence of a comparable locomotor-to-ocular motor coupling in the mouse. In neonates, *ex vivo* nerve recordings of brainstem-spinal cord preparations reveal a spino-extraocular motor coupled activity similar to the one described in Xenopus. In adult mice, trans-synaptic rabies virus injections in lateral rectus eye muscle label cervical spinal cord neurons closely connected to abducens motor neurons. Finally, treadmill-elicited locomotion in decerebrated preparations[7] evokes rhythmic eye movements in synchrony with the limb gait pattern. Overall, our data are evidence for the conservation of locomotor-induced eye movements in vertebrate lineages. Thus, in mammals as in amphibians, CPG-efference copy feedforward signals might interact with sensory feedback to ensure efficient gaze control during locomotion.

Citation: França de Barros et al., 2022, Current Biology 32, 453–461 ; January 24, 2022 © 2021 Elsevier Inc.

Results

Fictive locomotor activity induces ex vivo spino-extraocular motor coupling in neonates in absence of sensory inputs

The ability of locomotor CPG rhythmic activity to elicit a spino-extraocular motor coupling was evaluated on isolated *ex vivo* brainstem-spinal cord preparations of neonatal mice (Figure 1A). Electrical stimulation of either the first sacral dorsal root (S1Dr, Figure 1A) or the 8th cervical dorsal root (C8Dr, Figure S1A-B) evoked episodes of fictive locomotion with the typical coordination pattern between cervical and lumbar ventral roots (Vr) rhythmic activity (Vr; Figure 1A), as previously reported[8,9]. In accordance with this typical locomotor pattern, the example shown in Figure 1A demonstrates a paired bursting discharge between the homolateral C8 (light green in Figure 1A, bottom panel in B) and L2 (orange in Figure 1A, B bottom panel) Vr[8]. In most cases (66%, Figure 1C) this rhythmic cervico-lumbar coordinated locomotor activity was coupled to a bursting activity of the abducens motor nerves (Figure 1A-B) within the same frequency range (0.5-1.5Hz; Figure1D, E) and a latency of ~62ms to C8 Vr burst and ~80ms to L2 Vr burst, respectively (Figure 1F), compatible with a monosynaptic delay[10–12]. Inversely, non-coordinated spinal activity failed to evoke a coupled rhythmic discharge in the abducens nerves (Figure 1C). Locomotor-related bursts of an abducens nerve were synchronized to the ipsilateral C8-L2 Vr discharge (Figure 1B, bottom panel and Figure G), and alternated with the contralateral abducens discharge (Figure 1B, top panel).

Coordinated fictive locomotor episodes evoked by NMDA/5HT spinal immersion also produced a well correlated rhythmic activity in the abducens motor nerves (Figure S1C-F) in a lower frequency range (0.15-0.25Hz; Figure S1E) and with a preserved phase relationship relative to the Vr burst discharge (Figure S1F). In addition, frequency analysis of abducens discharge in response to S1Dr stimulation (Figure S1G-I) demonstrated that the spino-extraocular coupling was not induced by proprioceptive feedback inputs. Since all these brainstem-spinal preparations lacked visuo-vestibular sensory inputs as well as cortical, mesencephalic, and cerebellar inputs (see methods), the spino-extraocular motor coupling was produced by a locomotor efference copy signal, originating from the spinal motor CPGs.

Citation: França de Barros et al., 2022, Current Biology 32, 453–461 ; January 24, 2022 © 2021 Elsevier Inc.

Spino-extraocular motor coupling depends on the integrity of the cervical, and not lumbar, spinal cord

To determine the respective roles of the cervical and lumbar CPG networks in the origin of locomotor-induced spino-extraocular motor coupling, following the experimental approach previously used in xenopus[3], cervical and lumbar regions were selectively isolated in brainstem-spinal cord preparations using spinal split-baths (Figure 2A). When synaptic transmission in the cervical cord was blocked with calcium-free aCSF[9,12] (Figure 2A, left), electrical stimulation of the S1Dr evoked typical alternated fictive locomotor activity in the lumbar Vr (Figure 2B bottom red traces, Figure 2D upper panel). However, it failed to evoke correlated fictive locomotor activity in the cervical Vr or rhythmic discharge in the abducens motor nerves (Figure 2B upper blue and green traces, Figure 2D, lower panel). This experiment demonstrates the instrumental role of the activity of the cervical motor networks in the genesis of the spino-extraocular motor coupling.

Next, we tested whether the cervical cord acted as a neuronal relay, or whether it was the origin of the spino-extraocular motor coupling. Locomotor-induced rhythmic discharge of abducens motor nerves was recorded in response to electrical stimulation of either S1Dr or C8Dr, in isolated *ex vivo* preparations exposed to a complete mid-thoracic section (Figure 2E). After the thoracic section, S1Dr stimulation failed to produce any spino-extraocular motor coupling (Figure 2F) whereas C8Dr electrical stimulation evoked locomotor-induced rhythmic discharge of the abducens motor nerves (Figure 2G). Even though the cervical CPG-related abducens rhythmic activity was recorded at relatively low frequency (Figure 2H, 0.2-0.35Hz, orange circles), it remained in synchrony with C8Vr bursting discharge (Figure 2I and 2J). Overall, these results show that, while the activation of the lumbar CPG allowed for a more robust coupling, the locomotor-related activity of the abducens motor nerves specifically originated from the cervical CPG.

Cervical neuronal relay implicated in the spino-extraocular coupling

To determine the cervical neuronal relay involved in the spino-extraocular coupling (Figures 1 and 2), transsynaptic retrograde tracing of neuronal populations was performed by rabies virus (RV) injection in the lateral rectus muscle (LRM) of adult mice (Figure 3A). 55h after RV infection of motoneurons innervating the LRM (Figure 3A and 3B; see methods), several neuronal populations closely related to RV$^+$ abducens motoneurons (visualized by ChAT immunolabeling, Figure 3B-D) were labelled. As expected, based on the vestibulo-ocular reflex circuitry[13,14], RV$^+$ neurons were found in the vestibular nuclei (VN, Figure 3C) and contralateral oculomotor nucleus (contra nIII, Figure 3D). Moreover, RV$^+$ neurons were observed bilaterally throughout the cervical spinal cord (Figure 3E-F) in all preparations (n = 3; Figure 3G-I). The average RV infection ratio was of 1 abducens motoneuron contacted by 6 cervical neurons (Figure 3J). RV$^+$ cervical neurons were mainly located in the spinal ventral horn or around the central canal (Figure 3E-G and K). Notably, at this 55h labeling time window, no RV$^+$ neurons were observed caudally from the C8 segment. An extended infection time of 70h, which labelled extended network (Figure S3A) as e.g. cerebellum (Figure S3C) revealed spinal neuronal populations polysynaptically connected with abducens motoneurons (Fig S3B), scattered throughout the gray matter as well as beyond the cervical region (Figure S3D-G). The presence of RV$^+$ neurons in the dorsal horn (Figure S3E) suggests that brainstem-projecting spinal cord interneurons not only receive inputs from CPG but also putatively from sensory networks (Figure S3A). With this infection time (70h), rare RV$^+$ INs were detected in the rostral part of the lumbar spinal cord (L1-L2, n = 1 mouse, data not shown), whereas no RV$^+$ lumbar neurons were visible in lumbar spinal cord after 55h of infection (n = 3 mice). Overall, the use of RV trans-synaptic injections revealed a spinal-brainstem pathway likely to support the functional coupling of abducens motor nerve discharge with the rhythmic activity evoked by the cervical-CPG during locomotion in mice.

Coupling between forelimb and eye movements in decerebrated preparations

To determine if locomotor-induced eye movements occur *in vivo* in the absence of visual and vestibular sensory signals, eye movements were recorded in the dark during head-fixed treadmill locomotion in decerebrated adult mice (Figure 4A and Figure S4A). Such preparations enable the study of the spinal cord output and sensorimotor integration in the absence of descending cortical motor commands[7]. Figure 4A displays a representative example of the combined occurrence of locomotion and eye movements. Binocular nystagmic-like eye movements were observed during treadmill-evoked bouts of 10-40s sustained locomotion, after a >2hz locomotion was reached (Figure 4A, area in between the green arrows). This locomotor-induced oculomotor behavior consisted of an alternation of short

Citation: França de Barros et al., 2022, Current Biology 32, 453–461 ; January 24, 2022 © 2021 Elsevier Inc.

ocular movements (quick-phase like) in one direction, followed by longer eye movements (slow phase-like) of comparable amplitude in the opposite direction (Figure 4A-C; additional examples in Figure S4B). Eye movements were mostly restricted to the horizontal plane (compare vertical, in light colors, and horizontal components, in dark colors, in Figure 4B and 4C) and their orientation (Figure 4D) remained homogeneous throughout the recordings. Left and right eye movements were always conjugated, with similar directionality for both eyes, and appeared well coordinated (see quick and slow eye movement phases on mean cycles of panel C; horizontal binocular coordination on oculogram in Figure 4E). To determine the temporal relationship between locomotor and ocular movements, the occurrence of the limbs (left stance onset) and eye events (quick phase-like peak velocity) during this sequence were compared. The frequency of the oculomotor cycles increased with the frequency of the locomotor cycles (Figure 4F). Moreover, eye and forelimb movements were generally synchronized (Figure 4G). All preparations (n=5) shared two main features: first, consistent eye movements only occurred once a locomotion frequency above 1Hz was attained (Figure 4H, I)[15]. Second, the quantification of the event occurrence, comparing eye, forelimb and hindlimb movements, showed a match between eye and limb movements in about 80% of the cycles (Figure 4I, left bars), and an eye mismatch (limb movement, no eye movement; Figure 4I, middle bars) in about 20% of the cycles. Notably, locomotor-induced eye movements never occurred in the absence of forelimb movements (Figure 4I, right bars). Analysis of sequences with a ratio of forelimb/eye events near unity (see methods) revealed that the frequency of the eye movement was closely correlated with the frequency of the forelimb (Figure 4J, left panel), while locomotor and oculomotor cycles were well synchronized (Figure 4J, right panel). Left and right eye movements were tightly correlated and synchronized ($r^2 = 0.98$; Figure 4K; phase in right panel). In all recordings, eye movements consisted of nystagmic-like movements composed of alternated quick (0.066 ± 0.022 s) and slow (0.223 ± 0.095 s) duration phases (Figure 4L, left panel) lasting 20% and 80% of the oculomotor cycles, respectively (Figure 4L, right panel). Both components had similar amplitudes in range 1-8° (Figure 4M, quick phases - black, slow phases - gray, and Figure S4C), leading to different velocities (amplitude/velocity relation on Panel M; slopes of 20.27 and 2.09 for short and long duration eye movements, respectively; Figure S4C, right panel). Overall, eye movements were observed during >80% of trot-like locomotor cycles and closely matched forelimb movements. Thus, the results obtained in decerebrated preparations suggest the presence of a spino-extraocular motor

Citation: França de Barros et al., 2022, Current Biology 32, 453–461 ; January 24, 2022 © 2021 Elsevier Inc.

coupling based on an efference copy from the locomotor cervical CPG in adult mice, as described in newborn mice (Figures 1 and 2). Additionally, they demonstrate that the persistence of this functional short-latency pathway in adults (Figure 3) enables a tight coupling between forelimb locomotor movements and eye movements during sustained high dynamic (>2Hz) locomotion (Figure 4).

Citation: França de Barros et al., 2022, Current Biology 32, 453–461 ; January 24, 2022 © 2021 Elsevier Inc.

Discussion

Conservation of locomotor-induced spino-extraocular motor coupling through vertebrate evolution

Locomotor-induced spino-extraocular motor coupling was initially described in the Xenopus frog[2–6]. During swimming, both larvae and adult frogs exhibited a CPG efference copy-based extraocular bursting activity tightly coupled to the spinal motor rhythmic discharge. This spino-extraocular motor coordination adapted through metamorphosis to produce appropriate horizontal eye movements that counteracted either tail (larva) or limb (adults) movements during strong propulsive swimming[4–6]. The efference copy mechanism was supported by an ascending spinal-brainstem neural pathway connecting spinal cord neurons to extraocular motoneurons, crossed in larvae and bilateral in adult xenopus[3,4,5]. Using newborn and adult mice preparations, the present study reports a locomotor-induced spino-extraocular motor functional coupling that exhibits common features with the one found in frogs. First, in both species this coupling is supported by a spino-extraocular pathway that persists throughout ontogeny. Second, the bilateral distribution of cervical neurons revealed in mice by RV tracing suggests a comparable organization of the spinal-brainstem pathway between adult frog and mouse. Third, the locomotor-induced ocular signal, recorded either *ex vivo* or in decerebrated mice, was only observed during sustained and vigorous locomotor activity, corresponding to running behavior, a terrestrial equivalent for propulsive undulatory swimming. *Ergo*, our findings, combined with previous studies in Xenopus, strongly support the hypothesis that the CPG efference copy-based ocular signal is a conserved mechanism from amphibians to mammals, and putatively in other vertebrates. This locomotor-induced ocular behavior is in accordance with the absolute necessity to stabilize the visual field during motion, by performing rapid counteracting eye adjustments in all vertebrates, including humans[16]. There is considerable behavioral evidence for the contribution of locomotor-related spinal signals during gaze stabilization in several mammalian species. In cats[17,18] and in humans[19,20], locomotor signals are integrated to favor vertical eye movements by projecting gaze towards the direction of locomotion and canceling VOR during walking or running on a treadmill. In monkeys performing circular running in the dark, compensatory horizontal eye movements are favored by non-vestibular velocity signals[21]. Here, we report new evidence demonstrating the

Citation: França de Barros et al., 2022, Current Biology 32, 453–461 ; January 24, 2022 © 2021 Elsevier Inc.

existence of the spino-extraocular motor command in mice that could constitute a neural mechanism sustaining the coupling of locomotion to eye movements, as suspected in other mammalian species[20].

Functional considerations regarding the coupling of locomotion and eye movements in mice

In all vertebrates, gaze control largely results from the sensory-motor transformations which primarily depend on the integration of visual and vestibular inputs (optokinetic and vestibulo-ocular reflex)[22]. Interestingly, no locomotor-induced ocular movements were observed in head-fixed alert mice during sustained treadmill locomotion in the dark (Figure S4D), suggesting a sensory-dependent supraspinal control of the CPG efference copy signal in natural conditions, which is suppressed in decerebrated mice. Recent studies in mice reported that the vestibulo-ocular reflex accounts for a dominant part of the conjugated gaze stabilization observed during head-free locomotion[23–25]. VOR-based eye movements were found to reach higher dynamics, compensating naturalistic head movements interspersed with non-conjugated (vergence) and shifting movements relocating gaze during directed head turn[25,26]. The participation of the spino-extraocular motor coordination in the different repertoire of eye movements during natural locomotion remains to be determined. Nonetheless, our data provide clues regarding its physiological characteristics. First, regarding the pathway involved, viral tracing experiment revealed brainstem-projecting neurons in the motor ventral horn of the cervical spinal cord, which likely convey the locomotor efference copy signal to ocular motor neurons. Additionally, an extended time window demonstrated, in one preparation, connected neurons in the sensory dorsal horn, suggesting the potential integration of sensory and motor information by the spino-extraocular circuitry, which will require further confirmation. The restriction of infected neurons in the cervical segments at both short and extended time window, and tight coupling between forelimb and eye movements suggest that this coupling could produce ocular adjustments in response to the movements of the rostral part of the body (forelimb, shoulder girdle, neck, head). Second, regarding the necessary conditions for the coupling to occur, in the in vitro neonatal preparation the spino-extraocular coupling was consistently observed at frequencies <2Hz. However, in the adult decerebrated preparation, eye movements were observed when sustained locomotion reached frequency >2Hz. This disparity likely reflects differences in the age and/or preparation. Nevertheless, we cannot

Citation: França de Barros et al., 2022, Current Biology 32, 453–461 ; January 24, 2022 © 2021 Elsevier Inc.

exclude that the efference copy would already contribute to gaze control at subthreshold levels, during low dynamic locomotion which in decerebrated mice did not produce a tight coupling between forelimb and eye movements. This observation suggests that the spinal circuits driving the forelimb and ocular motor neurons are independent. However, both might be controlled by a common motor network whose activity would determine the efficacy of the coupling between forelimb and eye movements when high-dynamic locomotion is produced, as previously suggested[1]. Third, concerning the functional role of the efference copy, because the eye movements observed were restricted to the horizontal plane, this mechanism could serve as an additional signal complementing the VOR to stabilize gaze during horizontal whole-body turn or lateral deviations of the head. Alternatively, and as proposed for vertical VOR in humans, it could serve as a feedforward signal to anticipate the horizontal perturbation of gaze provoked during quadrupedal running. In sum, data reported here suggests that spino-extraocular motor coupling might, in the mouse, complement the visuo-vestibular based reflexes, accounting for the biomechanical coupling between the rostral part of the body and horizontal eye movements during high-dynamic locomotor patterns. All in all, the comparison of the mouse and the xenopus concerning the biomechanical constraints, type of locomotion, and changes during development suggests an adaptation of the CPG efference copy-based mechanism through the vertebrate lineages in relation with changes in sensory capacities and locomotor repertoire during evolution.

Citation: França de Barros et al., 2022, Current Biology 32, 453–461 ; January 24, 2022 © 2021 Elsevier Inc.

Acknowledgements

The authors thank Patrice Jegouzo for his technical help designing the set up for the semi-intact experiments, Patrice Coulon for his input on the rabies virus tracing and the Animotion collaborative platform (INCIA) for the help in the analysis of locomotion.

FFB, CT, MT & MB were supported by the Centre National d'Etudes Spatiales, the Centre National de la Recherche Scientifique, the Université de Paris, and by the Agence Nationale de la Recherche (ANR-15-CE32-0007-02).

JBC, GC, CT, DC & FML were supported by the Centre National de la Recherche Scientifique and the Université de Bordeaux, the Fondation pour la Recherche Médicale (DEQ20170336764) and by the Agence Nationale de la Recherche (ANR-15-CE32-0007-02).

This study contributes to the IdEx Université de Paris ANR-18-IDEX-0001.

This work has benefited from the support and expertise of the animal facility of BioMedTech Facilities at Université de Paris (Institut National de la Santé et de la Recherche Médicale Unité S36/Unité Mixte de Service 2009).

Author contribution

Conceptualization: FFB; FML, DC, MB. Methodology: FFB; MM, JBC, MT, HB, FML, MB. Software: JBC, MM, MT. Formal analysis: FFB; JBC, MT, CT; MM, FML, MB. Investigation: FFB; CT, MM, HB. Writing original manuscript: FFB; JBC, FML, MB. Writing review and editing: FFB; MM, JBC, MT, HB, FML, MB. Visualization: FFB; HB; FML; MB. Supervision: HB; FML; MB. Project administration: DC, FML, MB. Funding acquisition: DC, FML; MB.

Declaration of interests

The authors declare no competing interests.

Original article can be found at: https://doi.org/10.1016/j.cub.2021.11.022
Citation: França de Barros et al., 2022, Current Biology 32, 453–461 ; January 24, 2022 © 2021 Elsevier Inc.

Figure Legends

Figure 1. Fictive locomotor activity evokes spino-extraocular motor coupling in neonatal brainstem-spinal cord isolated preparations.

(A) Left side, schematic of the neonatal mouse brainstem and spinal cord preparation with stimulated and recorded nerve roots. In all experiments C5, C8, L2 and L5 Vr were targeted, as main flexor (C5, L2) and extensor (C8, L5) motor nerve of fore- and hindlimbs[8,9], respectively. Preparations with recording of at least 3 of these 4 ventral roots were retained for analysis. Right side, Extracellular nerve recordings (raw traces in light gray, integrated traces in color) of the left (le, light blue) and right (ri, dark blue) abducens nerves (Abd.), the left and right 8th cervical roots (le C8, light green; ri C8, dark green) and the right 2nd lumbar ventral root (le L2, orange). Discharges recorded during an episode of fictive locomotion evoked by the electrical stimulation of the S1 dorsal root (stim. S1Dr) with a 4Hz pulse train (black vertical bars).

(B) Average cyclic modulation of the discharge activity (integrated trace) from the motor nerves shown in (A) over 10 consecutive fictive locomotor cycles. The right C8 trace (dark green) was used as the reference to determine locomotor cycles.

(C) Percentage of total (C8: 7 mice, 19 sequences; L2: 8 mice, 13 sequences) preparations with a coordinated fictive locomotor pattern coupled with a rhythmic abducens discharge (coord./rhyth, black histogram; 66%), with an absence of coordinated fictive locomotor pattern and an absence of rhythmic abducens discharge (non coord./non rhyth, dark gray histogram; 33%), with a coordinated fictive locomotor pattern and an absence of rhythmic abducens discharge (coord./non rhyth, light gray histogram; 1%), with an absence of coordinated fictive locomotor pattern and a rhythmic Abducens discharge (non coord./rhyth; 0%).

(D) Linear correlation in bursting frequencies between the left abducens (Abd) nerve discharge and the left C8 (green) (Abd vs C8, n = 7, R = 0.9567, Pearson test, p <0.0001; $r^2 = 0.9153$), or left L2 (orange) (Abd vs L2, n = 8, R = 0.9696, Spearman test, p <0.0001; $r^2 = 0.9400$) spinal ventral roots.

Citation: França de Barros et al., 2022, Current Biology 32, 453–461 ; January 24, 2022 © 2021 Elsevier Inc.

(E-F) Individual (empty circles) and mean (bars) ±SEM of the frequency linear regression (**E**, r^2) and the latency (**F**, milliseconds, ms) between firing bursts of the abducens nerve (Abd) and spinal ventral root (sp. Vr) discharges (Abd vs C8Vr in green, mean $r^2 = 0.75 \pm 0.06$, mean latency = 61.7 ± 7.2ms; Abd vs L2Vr in orange, mean $r^2 = 0.82 \pm 0.06$, mean latency = 79.6 ± 9.7ms) for each preparation, independently of the frequency.

(G) Circular plots showing the phase relationships between the firing discharge burst in the left abducens nerve and ipsilateral C8 ($\mu = 357.359^\circ \pm 2.213$; r = 0,936; n = 7) and L2 ($\mu = 354.288^\circ \pm 1.467$; r = 0.97, n = 8) and contralateral L5 ($\mu = 198^\circ \pm 5.04$; r= 0.868, n = 3) Sp. Vr. In this and all polar plots, the width of the wedges is 0.05.

Supplemental data related to figure 1 is available as Figure S1.

Figure 2. The efference copy signaling responsible for spino-extraocular motor coupling originates in cervical locomotor CPG.

(A) Left side, schematic of the neonatal mouse brainstem and spinal cord preparation with the recorded nerve root and the calcium free ($0Ca^{2+}$) aCSF split bath on the cervical cord. Extracellular nerve recordings (raw traces in light gray, integrated traces in color) of the right (ri, dark blue) abducens nerves (Abd.), the right 8th cervical roots (ri C8, dark green) and the right and left 5th lumbar ventral roots (ri L5, dark red; le L5, light red) discharges during an episode of fictive locomotion evoked by the electrical stimulation of the S1 dorsal root (stim. S1Dr) with a 4Hz pulse train (black vertical bars). In the control condition (**A**), during bath application of $0Ca^{2+}$ aCSF (**B**) restricted to the cervical spinal cord and after washout (**C**).

(D) Averaged cyclic modulation of the discharge activity (integrated trace) from the motor nerves shown in A (top panel, control condition) and B (bottom, $0Ca^{2+}$) over 10 consecutive locomotor cycles. The right L5 trace was used as the reference to determine locomotor cycles.

(E) Left side, schematic of the neonatal mouse brainstem and spinal cord preparation with the recorded nerve branches during the mid-thoracic section experiments. Extracellular nerve recordings (raw traces in light gray, integrated traces in color) of the right (ri, dark blue) and

Citation: França de Barros et al., 2022, Current Biology 32, 453–461 ; January 24, 2022 © 2021 Elsevier Inc.

left (le, light blue) abducens nerves (Abd.), the right 8th cervical roots (ri C8, dark green) and the right 5th lumbar ventral root (ri L5, dark red) discharges during an episode of fictive locomotion evoked by the electrical stimulation of the S1 dorsal root (stim. S1Dr) with a 4Hz pulse train (black rectangle). Responses for control (**E**), after mid-thoracic complete transection during an episode of fictive locomotion evoked by the electrical stimulation of the S1 dorsal root (**F,** stim. S1Dr) and after mid-thoracic section during an episode of fictive locomotion evoked by the electrical stimulation of the C8 dorsal root (**G**, stim. C8Dr) with a 4Hz pulse train.

(H) Linear correlation in bursting frequencies between Abducens (Abd) nerve discharge and ipsi C8 Vr discharge in response to stimulation of the S1Dr during control conditions (black empty circles, R = 0.9817, Pearson test, $p < 0.0001$, n = 3; r^2= 0.9637), and after the mid-thoracic section (orange filled circles) (R = 0.9983, Pearson test, $p<0.001$, n = 3; r^2 = 0.9966).

(I) Polar plots of the phase relationships between the abducens and C8Vr before (control, left) abd C8 ipsi before (µ = 345.161º±2.546; r = 0.974) abd C8 contra before (µ = 162.803±4 .285; r = 0.943) and after mid-thoracic section (after cut, right) abd C8 ipsi after cut (µ = 353 .912±2,463; r = 0.999), abd C8 contra after cut (µ = 177.873±4.909; r = 0.939) (n =3 mice). The phase relationship is conserved after the cut.

(J) Mean absolute latency time between the activity in the C8 Vr and the abducens nerve in control (52.96±4.51ms) and after cut (66.49±5.96ms). There was no significant difference in the delay observed before and after the mid-thoracic cut (t-test, p=0.1038, n=3).

Figure 3. Anatomy of the spino-extraocular pathway

(A) Depiction of the rabies virus (RV) injection protocol. RV injections were performed in the lateral rectus (Lat. rectus) muscle of the left eye. After 55h of RV infection, labeled neurons (red asterisks) were found in the abducens (Abd) motor nuclei, and in the closely connected structures. PC, Purkinje cells; VN, vestibular nucleus neuron; EC, efferent copy spinal neuron.

Citation: França de Barros et al., 2022, Current Biology 32, 453–461 ; January 24, 2022 © 2021 Elsevier Inc.

(B) Representation (top panel) of the location (red square) of the RV$^+$ neurons in the abducens nucleus (nVI) and its landmarks: geniculum of the facial nerve (g7) and the 4th ventricle IVth v). The bottom panel shows a fluorescence microscopy image (20x) of an RV+/ChAT$^+$ neuron (RV, red) and abducens motoneurons (Abd. MN, ChAT, green) 55h after the infection.

(C) Representation (top panel) of the location (red square) of the RV$^+$ neurons in the medial vestibular nucleus (MVN) 55h after the infection. The fluorescence microscopy image (bottom panel, 20x) shows RV$^+$ but ChAT$^-$ (left insets) vestibular nucleus (VN) neurons.

(D) Confocal microscopy image (20x magnification) of a brainstem sagittal slice of the oculomotor nucleus (nIII) showing RV$^+$ (red) but ChAT$^-$ (green) interneurons (INs; white arrowheads in e1 and e2,) contralateral to the inoculation side, while MNs (ChAT+) are not RV-infected.

(E) Fluorescence microscopy reconstructed image (5x magnification) of a cervical cross section showing RV$^+$ neurons in the ventral horn (white arrowheads and (**E1**)) as well as ChAT+ neurons (**E2**). c.c, central canal; DR, dorsal root.

(F) Example (20x magnification) of a RV$^+$ neuron located near the central canal (c.c), not ChAT+ (F, left bottom inset).

(G) Location of the RV$^+$ neurons after 55h of infection. RV$^+$ neurons were represented by colored dots in the different segments of the cervical spinal cord for each preparation (prep #1 cyan, prep#2 purple, prep#3 blue). Ipsi: cervical spinal cord side ipsilateral to the RV injected in the left lateral rectus muscle.

(H) Plot of the number of RV$^+$ neurons (nb of neurons, x axis) in ipsilateral and contralateral sides and location along (distance, millimeters, y axis) the rostro-caudal cervical (C1-C8) segments for each preparation (prep #1 cyan, prep#2 purple, prep#3 blue).

(I) Number of RV$^+$ motoneurons (MN, x axis) in the abducens motor nucleus and corresponding number of RV$^+$ brainstem-projecting cervical neurons (Brainstem-projecting) for each preparation (prep #1 cyan, prep#2 purple, prep#3 blue).

Citation: França de Barros et al., 2022, Current Biology 32, 453–461 ; January 24, 2022 © 2021 Elsevier Inc.

(J) Mean +/- SD (black circle, 6.83±3.33) of the infection ratio indicating the average of RV^+ brainstem-projecting cervical neurons labelled *per* RV^+ abducens motoneuron infected.

(K) Scheme of the spatial distribution of all the RV^+ brainstem-projecting cervical neurons, shown in (G), *per* lamina of the cervical spinal cord. Gray lines represent the superimposed limits of the gray matter from panel G, purple outlines represent the limits of the laminae on a typical cervical spinal cross-section.

Supplemental data related to figure 3 is available as Figure S3.

Figure 4. Locomotion-induced eye movements in adult mice

(A-E) Example of the eye movements observed during an episode of treadmill-induced locomotion. **(A)** Left (le Eye position, blue trace) and right (ri Eye position, red trace) horizontal movements are observed after the onset of locomotion. Rectangles represent the stance phases of the left forelimb (dark green) and left hindlimb (light green); gaps between rectangles represent swing phases; green arrows contain a bout of continuous locomotion with instantaneous frequency above 2Hz). Upper right inset, depiction of the set up used for recording eye movements in decerebrated mice. A video oculography camera recorded the movement of each eye and an infra-red camera tracked the movement of the limbs while mice ran on a motorized treadmill. **(B)** Segment of the recording (dotted rectangle, panel A) showing the horizontal (dark blue and red traces) and vertical (light blue and light red traces) components of the eye movements and the corresponding locomotor cycles of the left fore- and hindlimbs. **(C)** Average modulation (over 16 consecutive cycles) of the eye movements and limb stance phases shown in panel B. For horizontal ocular traces, right is up. **(D)** Oculogram showing the stable orientation of the left eye movement during the segment in panel B. The reported angle of 16.1º is expressed relative to the horizontal plane with head in a stereotaxic position (Hor.pos. vs Ver.pos, R= -0.8699, Spearman test, $p = 0.031$; $r^2 = 0.75$). **(E)** Right eye vs left eye horizontal components (le+ri eyes) (riHor.pos. vs leHor.pos, R =

Citation: França de Barros et al., 2022, Current Biology 32, 453–461 ; January 24, 2022 © 2021 Elsevier Inc.

0.7152, Spearman test, p = 0,47*;* $r^2 = 0.51$), showing comparable amplitude and synchronized movements.

(F-G) Analysis of the eye movements in panel **(A)**. **(F)** Relation between the instantaneous frequency of the forelimb (dark green dots) or the hindlimb (light green dots), and the left horizontal eye movements (Right eye vs left forelimb, R = 0.7248, Spearman test, $p < 0.001$; $r^2 = 0.5253$; Right eye vs left hindlimb, R = 0.3195, Spearman test, $p = 0.0852$*;* $r^2 = 0.1021$). **(G)** Polar plot of the phase coupling between the peak velocity of the left eye quick phase and forelimb (µ = 18.272º±8,61; *r* = 0.718).

(H-J) Relation between the eye and limb movements. **(H)** Cumulative distribution of the locomotor frequency measured from the left forelimb (le fore.) and left hindlimb (le hind.) movements (beginning of stance phase). Rhythmic eye movements were observed when locomotion frequency reached 2-4Hz, corresponding to trot-like gait (gray interval, n=5 mice). **(I)** Proportions of the locomotor cycle showing eye and/or limb movements (left forelimb- dark green; left hindlimb- light green). **J)** Correlation (left panel; Forelimb vs eye instantaneous frequency, R = 0.6569, Pearson test, $p < 0.0001$*;* $r^2 = 0.4315$) and temporal relationship (right panel; µ = 358.763º±16.106; r = 0.777) between the instantaneous frequency of the eye (peak velocity of quick phase) and forelimb movements (beginning of stance phase).

(K-M) Quantification of eye movements during locomotion. **(K)** Instantaneous frequency of the left and right eye movements. The degree of conjugation of the eye movements is reflected in the high linear correlation (left panel; left vs right eye instantaneous frequency, R = 0,9873, Pearson test, $p < 0.0001$*;* $r^2 = 0.9748$) between left and right eye frequency and the synchrony between them (right panel; polar plot; µ = 355.641º±7.53; *r* = 0.991). **(L)** Distribution of the duration of eye movements. The short phases of the eye movements only last up to 200 milliseconds and are mainly distributed around 100 milliseconds whereas, the long phase of the eye movements is scattered and distributed up to 400 milliseconds. Right panel shows the relative duration of short and long eye movements during each cycle. Short eye movements (dark gray) represent 20% of the cycle; long eye movements (light gray) 80% of the cycles. **(M)** Main sequence of the eye movements showing the amplitude-velocity relationship of short (dark gray; Amplitude vs velocity of short component of eye movements, R = 0.9169, Spearman test, $p = 0.00366$; $r^2 = 0.8395$) and long (light gray; Amplitude vs velocity of long

Original article can be found at: https://doi.org/10.1016/j.cub.2021.11.022
Citation: França de Barros et al., 2022, Current Biology 32, 453–461 ; January 24, 2022 © 2021 Elsevier Inc.

component of eye movements, R = 0.5412, Spearman test, $p < 0.00001$; $r^2 = 0.2929$) components of the eye movements.

Supplemental data related to figure 4 is available as Figure S4.

Original article can be found at: https://doi.org/10.1016/j.cub.2021.11.022
Citation: França de Barros et al., 2022, Current Biology 32, 453–461 ; January 24, 2022 © 2021 Elsevier Inc.

STAR Methods

Resource availability

Lead contact

Further information and requests for resources should be directed to M. Beraneck (mathieu.beraneck@univ-paris.fr).

Materials availability

This study did not generate any new materials or reagents.

Data and code availability

The datasets generated during this study are available at “Dataset_Barros_2021”, Mendeley Data, V1, doi: 10.17632/h8nbswgf95.1

Experimental model and subject details

Animals were used in accordance with the European Communities Council Directive 2010/63/EU. All efforts were made to minimize suffering and reduce the number of animals included in the study. All protocols were performed on C57/BL6J male mice. *Ex vivo* experiments were performed on neonate (2-3 days old; n = 23) following procedures specifically approved by the ethical committee for animal research of the University of Bordeaux. Experiments on adults (8–14 weeks) were approved by the ethical committee for animal research of the University of Aix-Marseille (n = 6) and of the university of Paris (n = 29).

Ex vivo brainstem-spinal cord preparations

The dissection protocol followed as previously detailed by Kasumacic[10]. Briefly, mice were deeply anesthetized by 4% isoflurane inhalation until the loss of the nociceptive reflexes. After being placed in Sylgard-coated Petri dish, they were decerebrated and eviscerated while submerged in an ice-cold (1º-5ºC) oxygenated (95% O_2 and 5% CO_2) artificial cerebrospinal fluid (aCSF) (in mM: 128 NaCl, 4.5 KCl, 2.5 CaCl2.2H2O, 1.0 $MgSO_4.7H_2O$, 1.2

Citation: França de Barros et al., 2022, Current Biology 32, 453–461 ; January 24, 2022 © 2021 Elsevier Inc.

$NaH_2PO_4.H_2O$, 5 Hepes, 25 $NaHCO_3$ and 11 D-glucose). In a dorsal view, a craniotomy was performed to expose and remove the cerebellum, and the abducens nerves were carefully cut so that they could be recorded. With a ventral approach, a full laminectomy was done to expose the spinal cord and all the dorsal and ventral roots of both cervical sides were cut so that the final brainstem-spinal cord preparation could be extracted. After removing the meninges, the preparation was fixed with the ventral side up and fixed to the Sylgard-coated dish with insect pins and bathed in oxygenated aCSF fluid at room temperature.

Fictive locomotion protocols and recordings

Isolated brainstem-spinal cord preparations had the distal ends of abducens nerves as well as bilateral spinal dorsal motor roots (sacral, lumbar or cervical) simultaneously recorded (Model 1700 AC amplifiers, A-M Systems, Carlsborg, US) with fire-polished borosilicate glass suction recording electrodes filled with aCSF solution. In all experiments C5, C8, L2 and L5 Vr were targeted, as main flexor (C5, L2) and extensor (C8, L5) motor nerve of fore- and hindlimbs[8,9], respectively. Preparations with recording of at least 3 of these 4 ventral roots were retained for analysis. The electrodes were connected to extracellular amplifiers and the analog signals recorded by an analog/digital interface (CED 1401; Cambridge Electronic Design, Cambridge, UK). Signals were amplified (x10000) and digitized at 10 KHz (CED 1401; Cambridge Electronic Design, Cambridge, UK), displayed and stored on computer with acquisition software (Spike 2, Cambridge Electronic Design) and finally analyzed off-line with customized scripts. Fictive locomotion was achieved in brainstem-spinal cord preparations either through electrical or pharmacological stimulation.

For electrical stimulation, the electrodes suctioning the dorsal roots were connected to a pulse generator (Grass stimulator); this allowed the delivery of pulse trains (4Hz for 10s, inter-stimulus interval of 0.25s and at least 5 minutes between pulse trains). The described pulse trains were delivered at the lumbar or at the cervical levels while the abducens nerves were recorded.

To obtain fictive locomotion through pharmacological stimulation, the *ex vivo* brainstem-spinal cord preparations (n = 2 mice) were bathed in an aCSF infused with glutamatergic receptor agonists; namely NMDA (7,5 µM) and serotonin (5-HT; 15 µM).

Citation: França de Barros et al., 2022, Current Biology 32, 453–461 ; January 24, 2022 © 2021 Elsevier Inc.

In a subset of experiments (n = 6 mice), the motor coupling was disrupted using a split-bath configuration that allowed reversibly isolating the brainstem from the spinal cord. Isolation was obtained by partitioning the recording chamber with two custom-made plastic walls that traversed the preparation cervical and lumbar regions with spinal split-baths. The cervical spine was immersed in an aCSF 0 Ca2+ solution, in order to completely block transmission at that level, while lumbar root stimulation was performed. This calcium free ACSF perfusion was shown to block local synaptic transmission, but not axons *en passage*[9,12]. In a subset of experiments (n= 7 mice), a complete section was made at the thoracic spinal cord in order to disconnect the lumbar locomotor network from the cervical locomotor network. In these preparations cervical and lumbar networks were then stimulated independently from each other.

Methods for tracing experiments

Rabies virus (RV) manipulation was done by vaccinated experimenters in a Biosafety level 2 facility. The virus (Challenge Virus Strain, CVS) was produced and concentrated as previously described[27]. Aliquots of the virus were stocked at -80ºC and thawed before use. Mice were anesthetized by an intraperitoneal injection of ketamine (Imalgene, 60 mg/kg) and xylazine (Rompun, 10 mg/kg) and deep anesthesia was confirmed by lack of response to interdigital pinching. The left extraocular muscles were exposed through an incision on the skin covering the mouse's eye, surrounding fatty tissue was removed and absorbable hemostatic gelatin sponges were used to curtail bleeding (Spongostan, Ethicon). After its identification, the lateral rectus muscle (LR) was isolated using small hooks and an injector cannula (gauge 33), linked to a 10µL Hamilton syringe, was inserted. 1µL of the RV was then slowly injected and the needle was left in place for an extra minute to prevent leaking[28,29]. Finally, the skin was closed using non-absorbable monofilament suture and mice were put back on their cages under a red light for post-surgery care. As in our previous studies using RV as retrograde transneuronal tracer to characterize synaptically connected networks in rodents after peripheral inoculations[10,11,28–30], we determined the time windows required to infect neurons connected monosynaptically or polysynaptically to abducens motoneurons, based on anatomical data. A 70h window displayed RV$^+$ neurons in the cerebellum (Purkinje cells; Figure S3C), but an absence of RV$^+$ neurons in the pontine nuclei (directly projecting to Purkinje cells, data not shown), compatible with disynaptic connections to that delay. When

Citation: França de Barros et al., 2022, Current Biology 32, 453–461 ; January 24, 2022 © 2021 Elsevier Inc.

the inoculation time was lowered to 55h the RV + interneurons were restricted to the brainstem (including INs in the medial vestibular nucleus (MVN, Figure 3C, Baker et al., 1969), contralateral oculomotor nucleus (3N, Figure 3D)[14], prepositus nucleus (Pr)[31], reticulotegmental nucleus of the pons[32] and cervical spinal cord, with no infection in the cerebellum, suggesting monosynaptic connections to that delay. In case of infection of MNs in other oculomotor nuclei than the abducens, resulting from leakage during inoculation of the virus, the animal was excluded.

Immunochemistry

After 55 or 70h of RV infection, animals were deeply anesthetized with ketamine (Imalgene, 60 mg/kg) and xylazine (Rompun, 10 mg/kg) and perfused intracardially with 20mL of 0.1M phosphate buffer saline (PBS) followed by 20mL of 4% paraformaldehyde (PFA). Immediately after, the brain was dissected coronally from the midbrain to the medulla oblongata and the spinal cord was removed in a single block. Tissue fixation was let for 4h at 4˚C in 4% PFA, subsequently cryoprotected in 20% sucrose during at least 24h and freeze embedded at -80ºC in Tissue Tek (Sakura, Zoeterwoude, The Netherlands). Transverse sections (30 µm thick) of the brainstem and cervical and lumbar spinal cord were serially cut in cryostat (Microm, Heidelberg, Germany), and two alternate set of sections were collected[29]. One set was placed into 48 well plates filled with cryoprotection liquid, and kept at -20°C, and the other set was mounted on poly-L-lysine-coated slides. These latter sections were first incubated in blocking solution (PBS, Triton X- 100, 0,2% bovine-serum albumin and normal donkey serum), to avoid nonspecific binding for 1h at room temperature and then left at 4˚C for 48h with the anti-RV phosphoprotein[29] and anti-choline acetyltransferase (ChAT) diluted 1:100 in the blocking solution. After being rinsed thrice in PBS, sections were incubated at room temperature with the secondary antibodies Alexa546 goat anti-mouse (Thermo Fisher Scientific) and Alexa488 donkey anti-goat (Thermo Fisher Scientific) at a 1:200 dilution for 2h. Finally, sections were rinsed two times with PBS and once with tap water before being mounted (Immu-Mount, Fisher Scientific) under coverslips.

To analyze the distribution of RV^+ neurons, the obtained sections were visualized under an upright light microscope (Axioscope, Carl Zeiss, Germany) equipped with a camera lucida. A CCD camera (AxioCam MR3, Carl Zeiss) adapted on this microscope, or the use of a laser

Citation: França de Barros et al., 2022, Current Biology 32, 453–461 ; January 24, 2022 © 2021 Elsevier Inc.

scanning confocal microscopy (LSM ZEISS 510 Meta) allowed to photograph areas of interest at various magnifications. These images were afterwards treated in ZEN (Carl Zeiss) imaging software where brainstem RV^+/$ChAT^+$ motoneurons and spinal cord RV^+ neurons were counted on each section and plotted from one out of two (60µm apart). Only neurons with visibly infected nuclei, determined by the presence of Negri bodies, were considered. The success of the viral infection was verified by the presence of double-positive RV^+ and $ChAT^+$ neurons on the abducens nucleus (Figure 3B). Abducens motoneurons simultaneously RV^+ and $ChAT^+$ were found in all mice (n = 3), ipsilateral to the injection site (left lateral rectus muscle), while motoneurons innervating other eye muscles (Figure 3B) were never marked, confirming the specificity of the infection.

Procedure for decerebration

Procedures for decerebration were previously described by Meehan and colleagues[7]. Briefly, mice were deeply anesthetized with isoflurane (2–3% in 100% O2) in an induction chamber, and then transferred to a heating pad on the surgery table with a nose cone to maintain anesthesia (1.5–2% in 100% O2). A rectal thermometer (Physiosuite, Kent Scientific) was used to monitor body temperature throughout the surgery as well as a pulse oximeter (MouseSTAT, Kent Scientific) to monitor O_2 saturation. Mice were then artificially ventilated via tracheostomy by blunt dissection; first the sternohyoid muscle was exposed, then the upper half of the fibrous membrane between two cartilages was cut and finally, the air delivery mode was quickly switched to ventilator mode (SomnoSuite, Kent Scientific) and a plastic endotracheal tube was inserted into the trachea. After confirming that the pCO2 levels were acceptable (>2.5%), the isoflurane was lowered to 1-1,2%. To avoid excessive bleeding during the decerebration, the left and right carotid arteries were bluntly isolated, ligatured and cauterized using an electric cauterizer (Change-a-tip cauteries, Bovie). The initial midline incision was sutured and, to avoid dehydration, 0.3 ml of sterile lactated Ringer's solution (Braun Medical) were injected subcutaneously. The mouse was placed in a stereotaxic frame and a superficial cut was made across the skin above the midline of the skull. Using a micro-drill (Foredom, David Kopf Instruments), the skull was scored, and the parietal bones removed. Decerebration was performed at the confluence of the sagittal and transverse sinus, perpendicular to the midline and at a 40±5º angle (Figure S4A). A surgical scalpel (no.10 blade; Fine Science Tools) was used to perform a swift and gentle slicing motion. The structures rostral to the incision were fully removed to obtain a premammillary and precollicular decerebration. Finally, a subcutaneous injection of Ringer's lactate (0.3 ml) was applied, and the isoflurane gas anesthesia was decreased to zero. Complete anesthesia withdrawal and muscular tonus occurred 10-20 minutes after isoflurane removal; PCO_2 levels rose consequently.

Videoculography and locomotion recordings and analysis

After the decerebration, mice were tightly secured using ear bars and a custom-made mouthpiece onto the motorized treadmill (Panlab, Harvard Apparatus). All recordings were performed in complete darkness. The locomotion was recorded using an infrared video camera (100Hz; Grasshopper3, FLIR Systems, Inc) fixed perpendicular to the left side of the body. To perform binocular video-oculography, the eyes of the mouse were illuminated with infrared emitters attached to 2 CCD cameras (120Hz; ISCAN, Burlington, MA) that were placed symmetrically on each side of the treadmill. Special care was provided to prevent eye dryness by regularly re-applying ophthalmic gel, to ensure that at least one eye could be tracked online. Eye video signals were processed online (ETL-200, ISCAN, Burlington, MA), sampled at 1kHz (CED 1401; Cambridge Electronic Design, Cambridge, UK) and recorded with Spike2 software. Online tracking of the eye movements with set-up fixed cameras allowed verifying the absence of head movements during the recordings. The video-oculography and locomotion cameras were synchronized using trigger signals generated using spike2 software. Locomotor cycles were tracked from the acquired videos using a markerless pose estimation (DeepLabCut)[33]. Eye movements and locomotion were analyzed offline using DataView software (W.J. Heitler, University of St.Andrews Scotland) at the Animotion collaborative core facility of the INCIA laboratory (CNRS UMR5287, Université de Bordeaux, http://www.incia.u-bordeaux1.fr/spip.php?rubrique193).

Overall, locomotion and eye movements were observed on a total of n = 26 preparations. Due to the experimental difficulties associated with the decerebrated mice, it was challenging to obtain preparations that would generate sustained, rapid, and well-coordinated locomotion. Additionally, the heavy surgery (long anesthesia; dehydration)[34] also impacted the possibility to track the pupil. However, for the preparations that fulfilled these quality criteria (n=6), all demonstrated the spino-extraocular coupling.

Citation: França de Barros et al., 2022, Current Biology 32, 453–461 ; January 24, 2022 © 2021 Elsevier Inc.

For locomotor analysis, the stance and swing phases of left forelimbs and hindlimbs, were defined based on the X, Y values issued from DeepLabCut pose estimation. Locomotor cycles were defined using the beginning of the stance phase of the left forelimb. The instantaneous frequency of locomotor cycles was calculated. Only sequences which exhibited bouts of sustained locomotion (>10 locomotor cycles) at frequency >1Hz were retained for analysis (n = 6). For oculomotor analysis, the position traces imported in DataView were integrated to obtain the velocity of the eye. The peak velocity of the alternated fast and slow phases of eye movements were detected using local peak detection. To analyze the coupling between limb and eye movements, beginning of locomotor cycles were defined as the onset of stance phase of the left forelimb. Oculomotor events were defined as the peak velocity of the quick phases. For each bout of locomotion, ratio of eye/limb events was calculated and sequences with a ratio in range 0.8-1.2 were retained. Analysis was then performed to compare the occurrence of both events, the instantaneous limb/eye frequency, and for each locomotor cycle, the correlation and temporal relation of limb (stance onset) and oculomotor (peak velocity of quick phase) events.

Quantification and statistical analysis

A table featuring all the numerical values obtained from the statistical tests performed is available as Table S1. Prism (GraphPad) was used for statistical analysis.

For paired t-tests normality was first evaluated using the D’Agostino & Pearson normality test and Shapiro-Wilk in the case of smaller unpaired two-tailed samples. When testing locomotion frequency and latency as well as the integrated electrophysiological signals, differences between two results were obtained using the unpaired two-tailed Mann–Whitney *U*-test and Kolmogorov–Smirnov test to compare distributions. To compare several values, the non-parametric Kruskal–Wallis test was processed with a Dunn’s multiple comparisons test. To evaluate the correlations between the frequencies of discharge of the locomotor nerves and the extraocular nerves, regression tests (R) and linear regression (r^2) were performed. Regression results were expressed as (R, r^2). Circular data was analyzed with Oriana 4.02 (Kovach Computing Services, UK) and the phase and strength of coupling were indicated by their mean vector (µ) and its length (r), respectively for non-uniform distributions values (tested with the Rayleigh's uniformity test, *p*).

Citation: França de Barros et al., 2022, Current Biology 32, 453–461 ; January 24, 2022 © 2021 Elsevier Inc.

The results are expressed as the mean ± SEM and *p* values threshold determined as $^{*}p < 0.05$; $^{**}p < 0.01$; $^{***}p < 0.001$; $^{****}p < 0.0001$; ns: non-significant.

Citation: França de Barros et al., 2022, Current Biology 32, 453–461 ; January 24, 2022 © 2021 Elsevier Inc.

References

1. Straka, H., Simmers, J., and Chagnaud, B.P. (2018). A New Perspective on Predictive Motor Signaling. Current Biology *28*, R232–R243.

2. Combes, D., Le Ray, D., Lambert, F.M., Simmers, J., and Straka, H. (2008). An intrinsic feed-forward mechanism for vertebrate gaze stabilization. Current Biology *18*, R241–R243.

3. Lambert, F.M., Combes, D., Simmers, J., and Straka, H. (2012). Gaze Stabilization by Efference Copy Signaling without Sensory Feedback during Vertebrate Locomotion. Current Biology *22*, 1649–1658.

4. Bacqué-Cazenave, J., Courtand, G., Beraneck, M., Lambert, F.M., and Combes, D. (2018). Temporal Relationship of Ocular and Tail Segmental Movements Underlying Locomotor-Induced Gaze Stabilization During Undulatory Swimming in Larval Xenopus. Front Neural Circuits *12*, 95.

5. Uckermann, G. von, Ray, D.L., Combes, D., Straka, H., and Simmers, J. (2013). Spinal Efference Copy Signaling and Gaze Stabilization during Locomotion in Juvenile Xenopus Frogs. J. Neurosci. *33*, 4253–4264.

6. von Uckermann, G., Lambert, F.M., Combes, D., Straka, H., and Simmers, J. (2016). Adaptive plasticity of spino-extraocular motor coupling during locomotion in metamorphosing Xenopus laevis. J Exp Biol *219*, 1110–1121.

7. Meehan, C.F., Mayr, K.A., Manuel, M., Nakanishi, S.T., and Whelan, P.J. (2017). Decerebrate mouse model for studies of the spinal cord circuits. Nature Protocols *12*, 732–747.

8. Juvin, L., and Morin, D. (2005). Descending respiratory polysynaptic inputs to cervical and thoracic motoneurons diminish during early postnatal maturation in rat spinal cord. Eur J Neurosci *21*, 808–813.

9. Juvin, L., Le Gal, J.-P., Simmers, J., and Morin, D. (2012). Cervicolumbar coordination in mammalian quadrupedal locomotion: role of spinal thoracic circuitry and limb sensory inputs. J Neurosci *32*, 953–965.

10. Kasumacic, N., Lambert, F.M., Coulon, P., Bras, H., Vinay, L., Perreault, M.-C., and Glover, J.C. (2015). Segmental Organization of Vestibulospinal Inputs to Spinal Interneurons Mediating Crossed Activation of Thoracolumbar Motoneurons in the Neonatal Mouse. Journal of Neuroscience *35*, 8158–8169.

11. Lambert, F.M., Bras, H., Cardoit, L., Vinay, L., Coulon, P., and Glover, J.C. (2016). Early postnatal maturation in vestibulospinal pathways involved in neck and forelimb

Citation: França de Barros et al., 2022, Current Biology 32, 453–461 ; January 24, 2022 © 2021 Elsevier Inc.

motor control: Vestibulospinal Projections to Cervical Spinal Cord in Neonatal Mouse. Developmental Neurobiology *76*, 1061–1077.

12. Brocard, F., Vinay, L., and Clarac, F. (1999). Gradual development of the ventral funiculus input to lumbar motoneurons in the neonatal rat. Neuroscience *90*, 1543–1554.

13. Horn, A.K.E., and Straka, H. (2021). Functional Organization of Extraocular Motoneurons and Eye Muscles. Annual Review of Vision Science *7*, 793–825.

14. Maciewicz, R.J., Kaneko, C.R., Highstein, S.M., and Baker, R. (1975). Morphophysiological identification of interneurons in the oculomotor nucleus that project to the abducens nucleus in the cat. Brain Res *96*, 60–65.

15. Lemieux, M., Josset, N., Roussel, M., Couraud, S., and Bretzner, F. (2016). Speed-Dependent Modulation of the Locomotor Behavior in Adult Mice Reveals Attractor and Transitional Gaits. Front. Neurosci. *10*.

16. Land, M. (2019). Eye movements in man and other animals. Vision Research *162*, 1–7.

17. Rivers, T.J., Sirota, M.G., Guttentag, A.I., Ogorodnikov, D.A., Shah, N.A., and Beloozerova, I.N. (2014). Gaze shifts and fixations dominate gaze behavior of walking cats. Neuroscience *275*, 477–499.

18. Zubair, H.N., Chu, K.M.I., Johnson, J.L., Rivers, T.J., and Beloozerova, I.N. (2019). Gaze coordination with strides during walking in the cat. J Physiol *597*, 5195–5229.

19. Dietrich, H., and Wuehr, M. (2019). Strategies for Gaze Stabilization Critically Depend on Locomotor Speed. Neuroscience *408*, 418–429.

20. Dietrich, H., and Wuehr, M. (2019). Selective suppression of the vestibulo-ocular reflex during human locomotion. J. Neurol. *266*, 101–107.

21. Solomon, D., and Cohen, B. (1992). Stabilization of gaze during circular locomotion in darkness. II. Contribution of velocity storage to compensatory eye and head nystagmus in the running monkey. J Neurophysiol *67*, 1158–1170.

22. França de Barros, F., Schenberg, L., Tagliabue, M., and Beraneck, M. (2020). Long term visuo-vestibular mismatch in freely behaving mice differentially affects gaze stabilizing reflexes. Sci Rep *10*, 20018.

23. Meyer, A.F., Poort, J., O’Keefe, J., Sahani, M., and Linden, J.F. (2018). A Head-Mounted Camera System Integrates Detailed Behavioral Monitoring with Multichannel Electrophysiology in Freely Moving Mice. Neuron *100*, 46-60.e7.

24. Payne, H.L., and Raymond, J.L. (2017). Magnetic eye tracking in mice. Elife *6*.

25. Michaiel, A.M., Abe, E.T., and Niell, C.M. (2020). Dynamics of gaze control during prey capture in freely moving mice. Elife *9*.

Citation: França de Barros et al., 2022, Current Biology 32, 453–461 ; January 24, 2022 © 2021 Elsevier Inc.

26. Meyer, A.F., O'Keefe, J., and Poort, J. (2020). Two Distinct Types of Eye-Head Coupling in Freely Moving Mice. Curr. Biol. *30*, 2116-2130.e6.

27. Gaudin, Y., Ruigrok, R.W.H., Tuffereau, C., Knossow, M., and Flamand, A. (1992). Rabies virus glycoprotein is a trimer. Virology *187*, 627–632.

28. Bras, H., Gaytán, S.P., Portalier, P., Zanella, S., Pásaro, R., Coulon, P., and Hilaire, G. (2008). Prenatal activation of 5-HT $_{2A}$ receptor induces expression of 5-HT $_{1B}$ receptor in phrenic motoneurons and alters the organization of their premotor network in newborn mice. European Journal of Neuroscience *28*, 1097–1107.

29. Coulon, P., Bras, H., and Vinay, L. (2011). Characterization of last-order premotor interneurons by transneuronal tracing with rabies virus in the neonatal mouse spinal cord. The Journal of Comparative Neurology *519*, 3470–3487.

30. Khalki, L., Sadlaoud, K., Lerond, J., Coq, J.-O., Brezun, J.-M., Vinay, L., Coulon, P., and Bras, H. (2018). Changes in innervation of lumbar motoneurons and organization of premotor network following training of transected adult rats. Experimental Neurology *299*, 1–14.

31. Escudero, M., and Delgado-García, J.M. (1988). Behavior of reticular, vestibular and prepositus neurons terminating in the abducens nucleus of the alert cat. Exp Brain Res *71*, 218–222.

32. Destombes, J., and Rouvière, A. (1981). Ultrastructural study of vestibular and reticular projections to the abducens nucleus. Exp Brain Res *43*, 253–260.

33. Mathis, A., Mamidanna, P., Cury, K.M., Abe, T., Murthy, V.N., Mathis, M.W., and Bethge, M. (2018). DeepLabCut: markerless pose estimation of user-defined body parts with deep learning. Nature Neuroscience *21*, 1281.

34. Lee, H., Kim, H.K., Shin, H.S., Han, S.J., Yoon, S., Seong, J.K., and Seo, K.Y. (2020). Evaluation of factors related to Anaesthesia-induced Lens opacity in experimental mice. Laboratory Animal Research *36*, 1.

França de Barros et al.
Figure 1

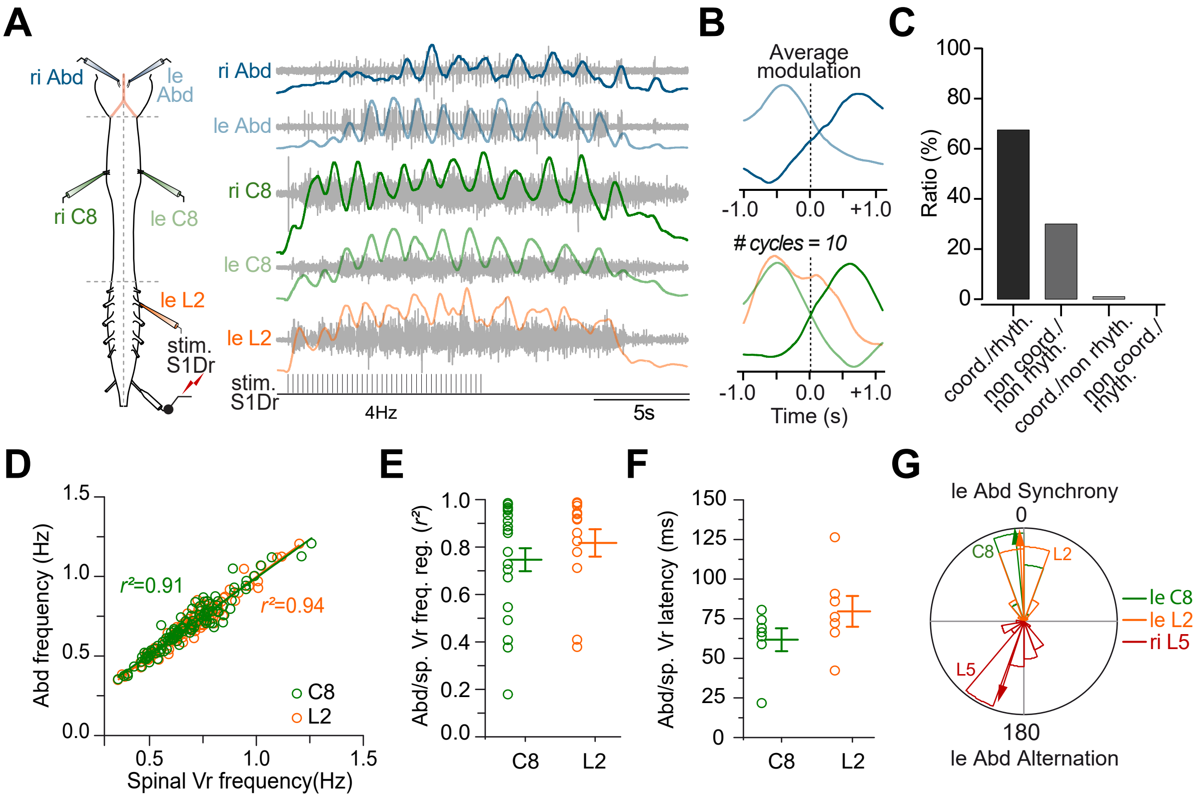

França de Barros et al.
Figure 2

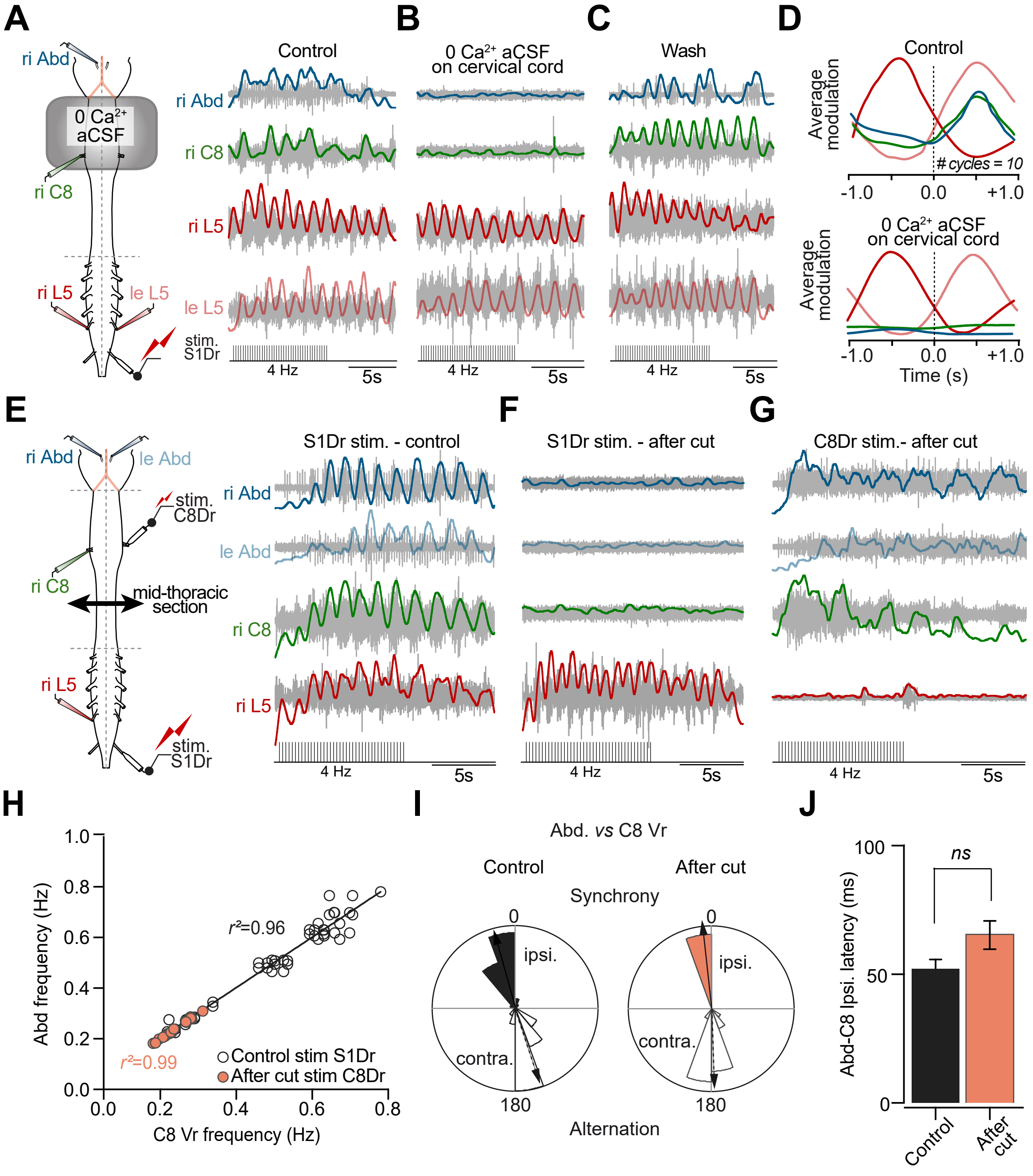

De Barros et al.
LOCOGAZE mouse
Figure 3 revision fml

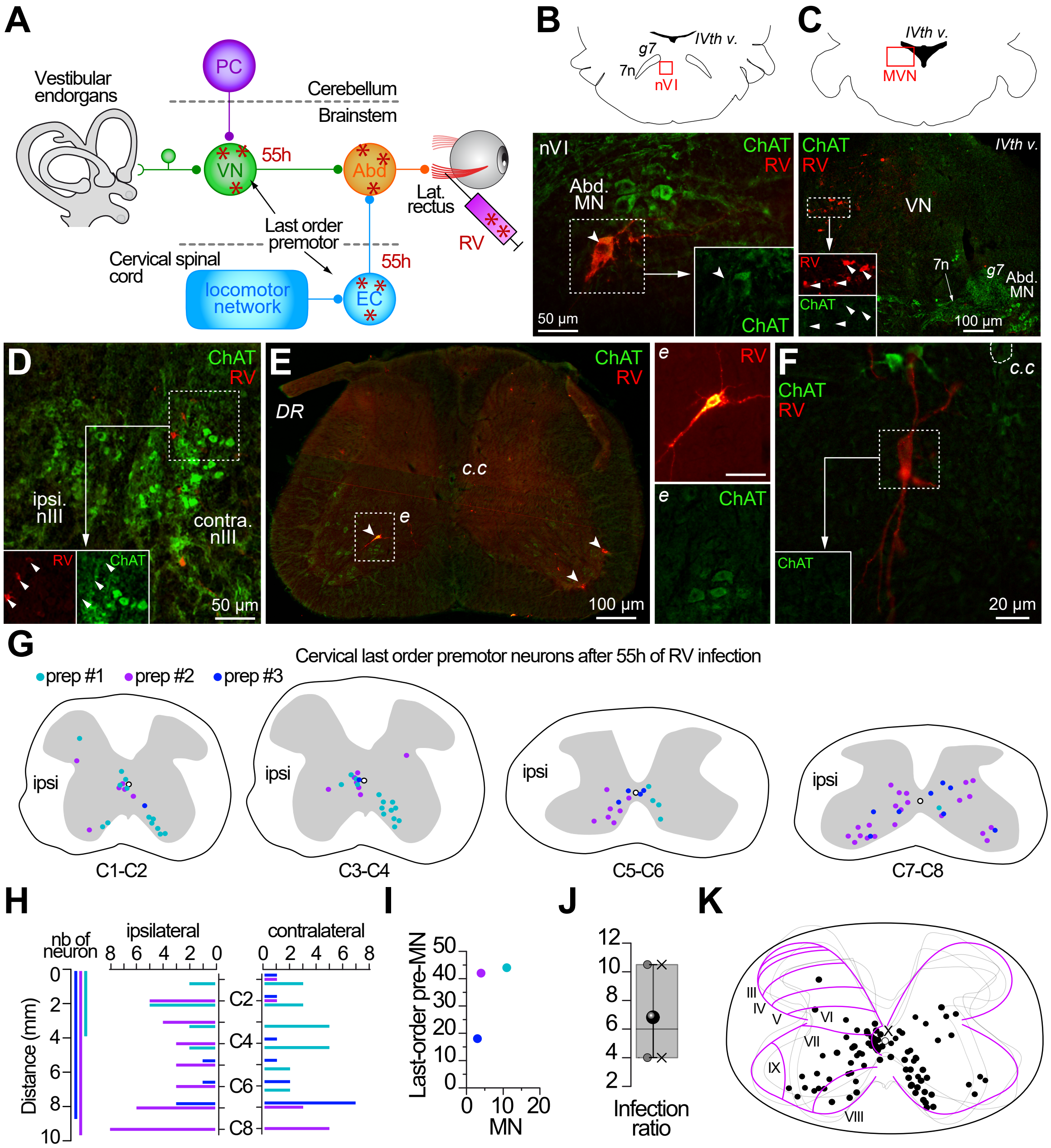

França de Barros et al.
Figure 4

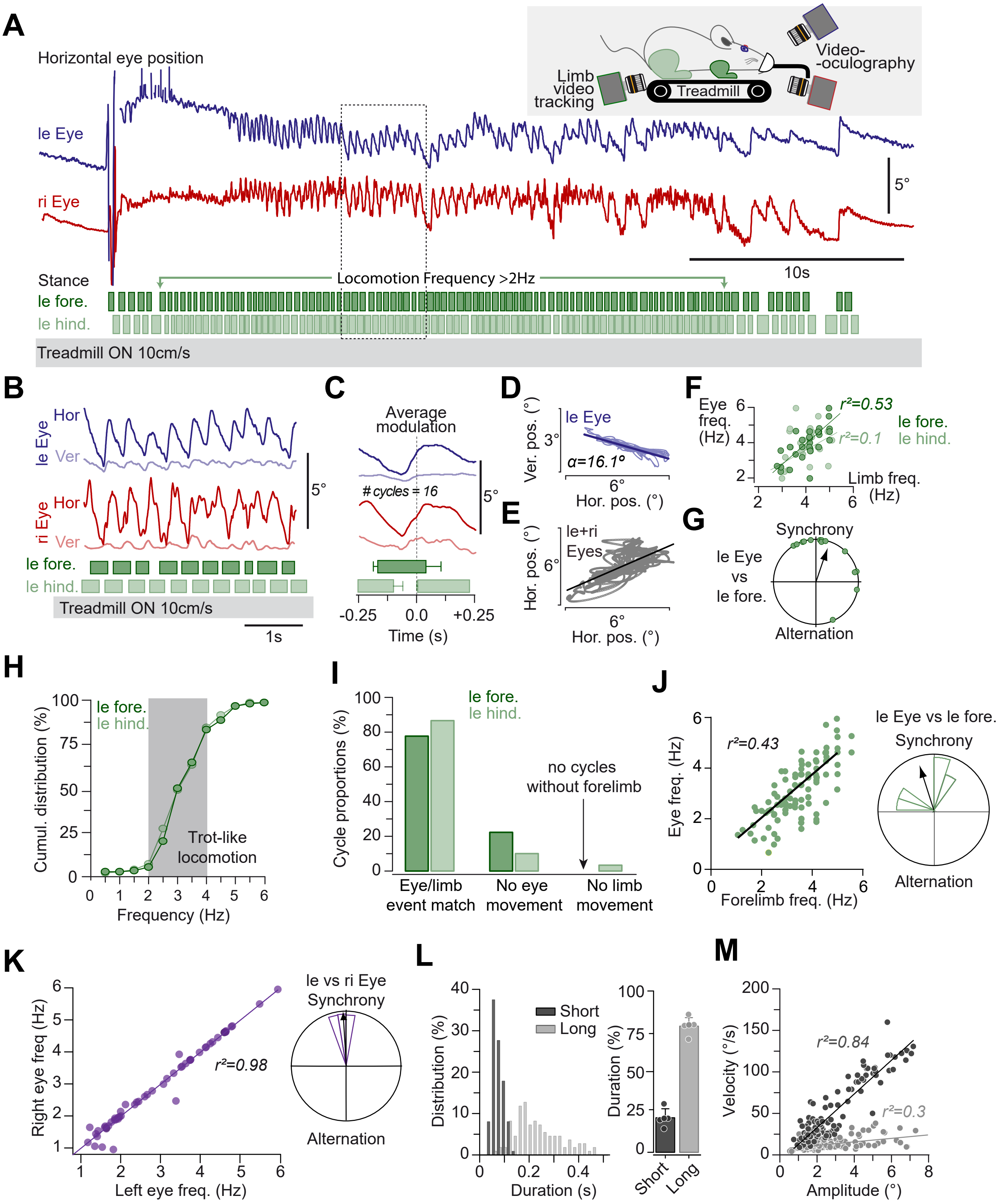

França de Barros et al.
Supplementary Figure 1

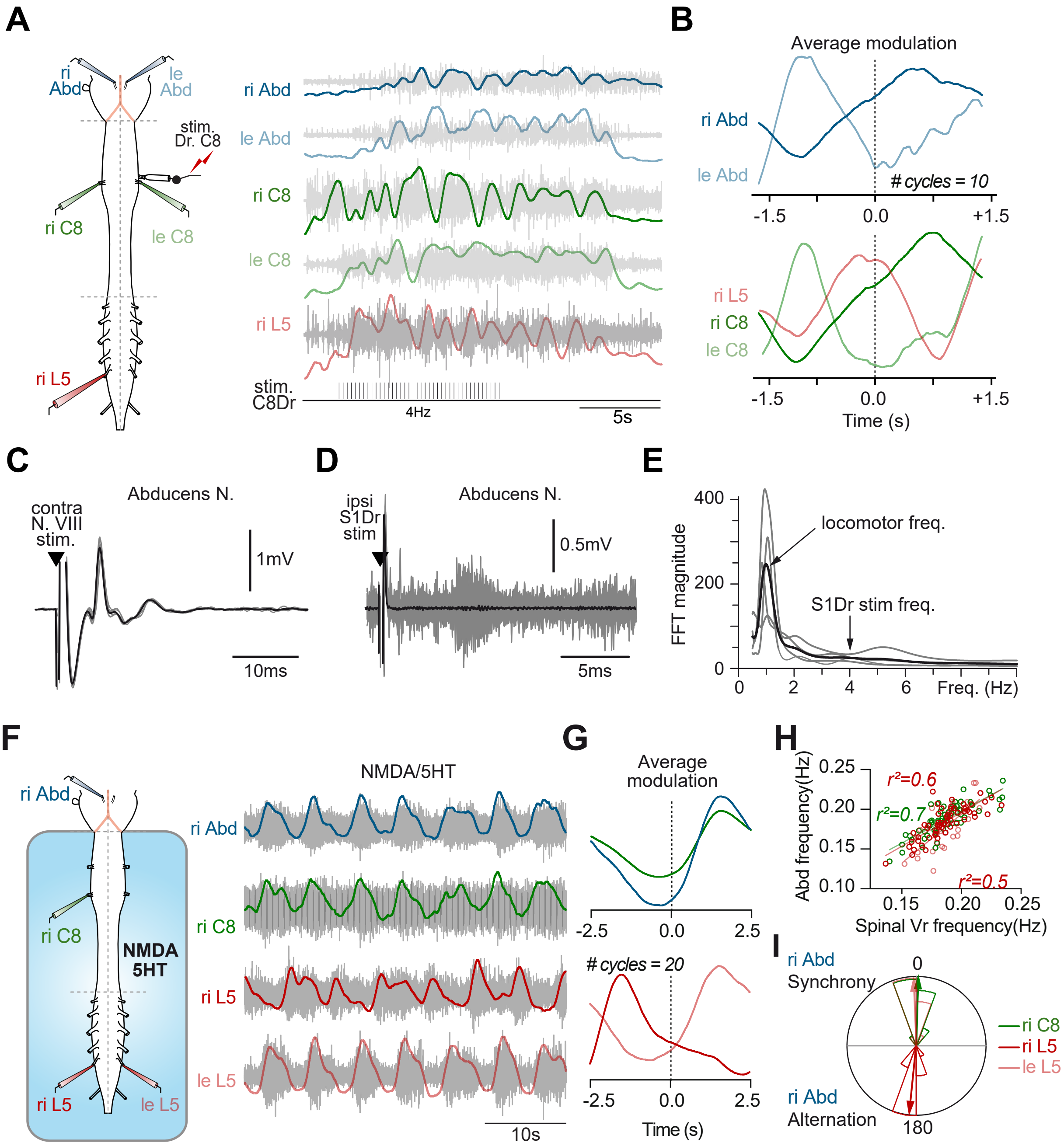

De Barros et al.
LOCOGAZE mouse
Figure S3

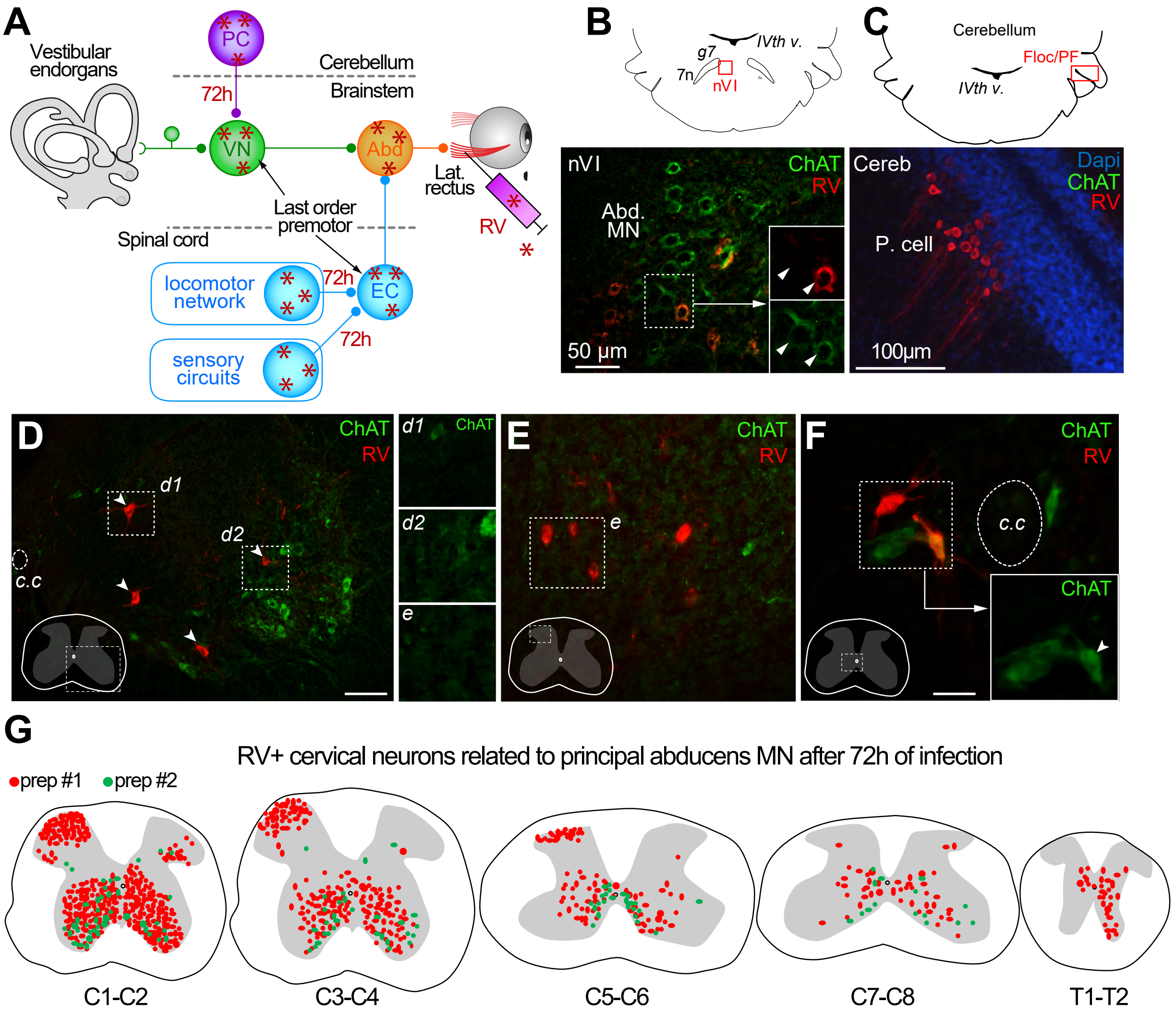

França de Barros et al.
Supplementary Figure 4

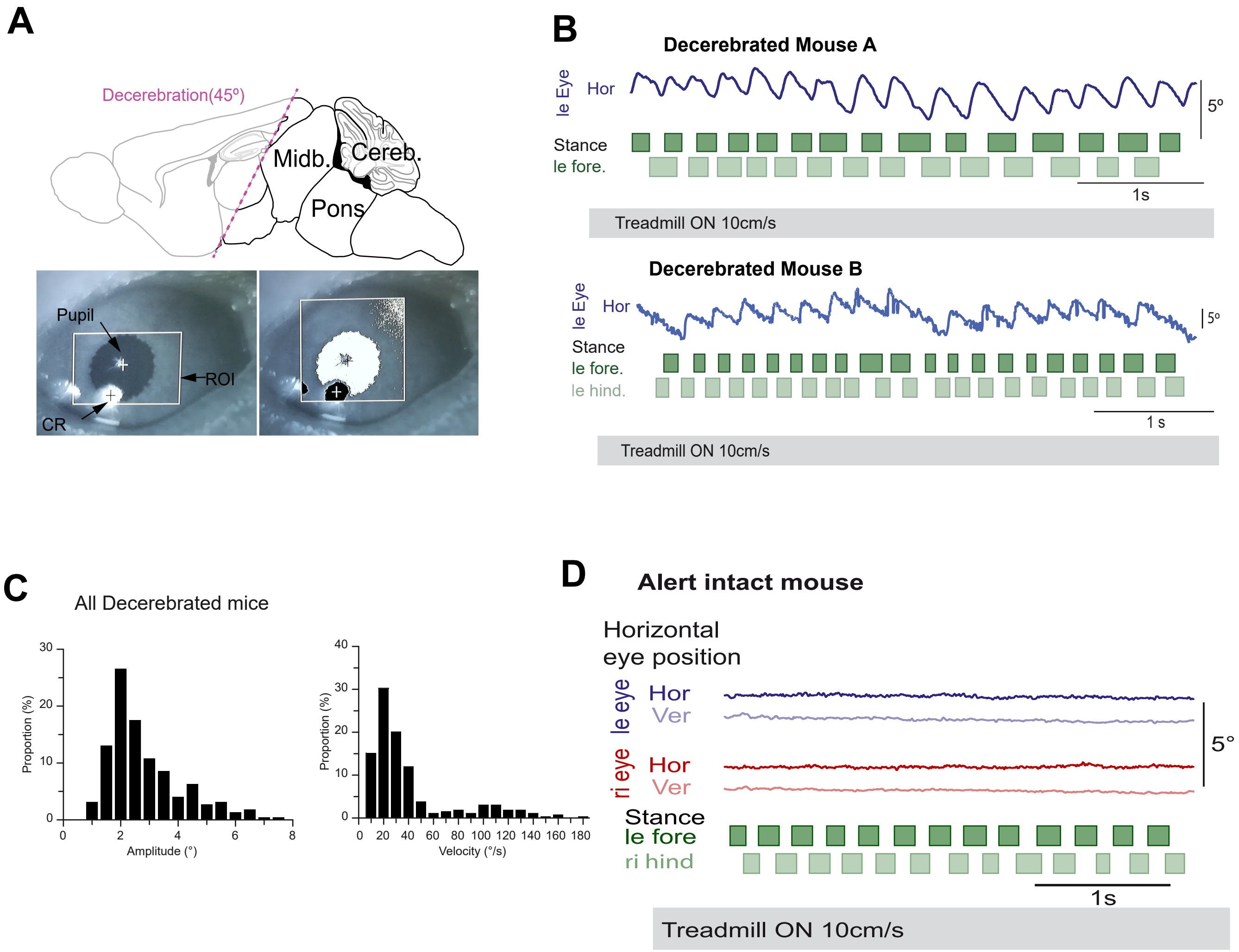

Supplementary Figure 1. Fictive locomotor episodes evoked by electrical and NMDA/5HT produce a rhythmic activity in the abducens motor nerves, irrespective of proprioceptive feedback inputs. Related to Figure 1 and 2.

(A) Fictive locomotion episodes evoked by cervical CPG stimulation. Left side, schematic of the neonatal mouse brainstem and spinal cord preparation with stimulated and recorded nerve branches. Right side, extracellular nerve recordings (raw traces in light gray, integrated traces in color) of the left (le, light blue) and right (ri, dark blue) abducens nerves (Abd.), the left and right 8th cervical roots (le C8, light green; ri C8, dark green) and the right 5th lumbar ventral root (ri L5, red). Discharges recorded during an episode of fictive locomotion evoked by the electrical stimulation of the C8 dorsal root (stim. C8Dr) with a 4Hz pulse train (bottom line).

(B) Average cyclic modulation of the discharge activity (integrated trace) from the motor nerves shown in (A) over 10 consecutive fictive locomotor cycles. The ri C8 trace (dark green) was used as the reference to determine locomotor cycles

(C) Left side, schematic of the neonatal mouse brainstem and spinal cord preparation with recorded nerve roots and NMDA/5HT split bath on the spinal cord. Right side, extracellular nerve recordings (raw traces in light gray, integrated traces in color) of the right (ri, dark blue) abducens nerves (Abd.), the right 8th cervical roots (ri C8, dark green) and the right and left 5th lumbar ventral root (ri L5, dark red; le L5, light red) discharges during an episode of fictive locomotion evoked by bath application of 5HT (15 µM) and NMDA (7,.5 µM) restricted to the spinal cord.

(D) Averaged cyclic modulation of the discharge activity (integrated trace) of the motor nerves shown in panel H over 20 consecutive locomotor cycles. The right C8 trace (green) was used as the reference to determine locomotor cycles.

(E) Linear correlation in bursting frequencies between the abducens (Abd) nerve discharge and ipsilateral C8 (green) (ri Abd vs ri C8, n = 2, R = 0.8187, Spearman test, $p < 0.0001$; $r^2 = 0.6702$), ipsilateral L5 (ri L5, red) (Abd vs L5, n= 2, R = 0.7879, Spearman test, $p < 0.0001$; $r^2 = 0.6208$) and, contralateral L5 (le L5, pink) (Abd vs L5, n = 2, R = 0.7045, Spearman test, $p < 0.0001$; $r^2 = 0.4964$) spinal ventral roots (Vr) discharges from the sequence shown in H.

(F) Circular plots showing the phase relationships between the discharge burst in the right abducens nerve and ipsilateral C8 (µ = 1.432º±2.52; r = 0.949), ipsilateral L5 (µ = 357.97º ±1.826; r = 0.9712) and contralateral L5 (µ = 185.835º± 2.273; r = 0.954) spinal ventral roots (n = 2 mice). The right C8 and the left L5 were in synchrony with the abducens nerve discharge while the right L5 was in alternation.

(G) VIIIth nerve-evoked (black arrowhead) abducens motor responses (individual traces in gray; mean in black) occur with a typical disynaptic latency compatible with the activation of the direct VOR pathway.

(H) Superimposed abducens discharge activity (gray traces) in response to electrical pulse applied on S1Dr (black arrowheads, as in figure 1A) and average activity (black trace). No reproducible dorsal root sensory-related response was observed following the S1Dr stimulation.

(I) Frequency periodograms obtained from FFT (Fast Fourier Transform) analysis of the abducens nerve discharge in response to S1Dr electrical stimulation evoking fictive locomotion episodes (Figure 1A and panel D) (gray traces represent a single locomotor sequence; the black trace is the average from the 4 gray traces). Periodograms revealed only one magnitude peak at the locomotor frequency (locomotor freq., about 1Hz) and did not show any peak at the S1Dr stimulation frequency (S1Dr freq., 4Hz), demonstrating the absence of spinal afference-evoked direct response in the abducens discharge.

Supplementary Figure 3. Extended connections of the spino-extraocular pathway 70h after a rabies virus inoculation. Related to Figure 3.

(A) Depiction of the RV labeling obtained 70h after RV inoculation in the lateral rectus muscle. RV^+ neurons are represented with red asterisks. Abd, abducens motor nuclei; PC, Purkinje cells; VN, Vestibular nucleus neurons; EC, efferent copy spinal neuron.

(B) Representation (top panel) of the location (red square) of the RV^+ neurons in the abducens motor nucleus (nVI) and its landmarks: geniculum of the facial nerve (g7, 7n) and 4th ventricle (IVth v.). The bottom panel shows a fluorescence microscopy image (20x) of a RV^+/$ChAT^+$ Abducens motoneuron (Abd. MN; RV, red; ChAT, green) 70h after the RV inoculation.

(C) Representation (top panel) of the cerebellar location (red box, Floc/PF: Flocculus/Paraflocculus) of the RV^+ Purkinje cells (P. cell) shown in the fluorescence microscopy image (bottom panel, 20x magnification) 70h after the RV infection.

(D, E, F) Fluorescence microscopy images of cervical spinal cord sections showing the ventral (**D**) (10x magnification), dorsal (**E**) horns (10x magnification) and around the central canal (c.c) (**F**) (20x magnification) location of RV^+ neurons. The RV^+ spinal cord neurons found in the ventral (**D1, D2** insets) and dorsal (**E1**) horns were not $ChAT^+$. However, some neurons found around the central canal (**F1**) were simultaneously RV^+ and $ChAT^+$.

(G) Scheme of the location of the RV^+ neurons found in the different cervical (C1-C8) and thoracic (T1, T2) segments following the 70h protocol. Red and green dots correspond to 2 different preparations (prep#1 red; prep #2 green). Variability in the labelling results from well-described methodological points[S1–S4]. Labeled neurons were found with a clear rostro-caudal gradient, in the ipsilateral and contralateral ventral horn, and in the ipsilateral dorsal horn of rostral cervical segments.

Supplementary Figure 4. Eye movements during head-fixed treadmill locomotion in decerebrated and intact adult mice. Related to Figure 4.

(**A**) Upper panel: scheme of the decerebration performed in adult mice. The 45º decerebration angle ensured a premammillary and precollicular decerebration; the structures outlined in black were preserved while the ones in gray were removed. Lower panel: (**A1**) picture of the right eye during a videoculography recording (see inset in Figure 4A) with region of interest (ROI) tracked; the pupil and corneal reflection (CR). (**A2**) shows the same eye with the detection threshold applied.

(**B**) Left eye movement traces and locomotor cycles of two additional decerebrated mice (A and B) running on a treadmill at 10 cm/s. As exemplified in Figure 4A-B, the horizontal (le Eye Hor, dark blue traces) and vertical (le Eye Ver, light blue traces) components of the eye movements are also shown for these mice. Rectangles represent the stance phases of the left forelimb (dark green) and left hindlimb (light green); gaps between rectangles represent swing phases.

(**C**) Distribution of the amplitude and velocity of the horizontal eye movements generated during treadmill locomotion in all decerebrated preparations (n= 5 mice).

(**D**) Eye movement traces and locomotor cycles of an intact mouse (head-fixed but not decerebrated) running on a treadmill at 10 cm/s in the dark. No horizontal (Leye; dark blue trace: horizontal, light blue trace: vertical) or vertical movements are observed after the onset of locomotion (dark green- left forelimb; light green- left hindlimb stance phases)

Figure #	Statistics									Data samples
	Panel	Data structure	Type of test	*p* value	R	r2	Mean	SEM	Length of mean vector	
1	D (L2. orange)	Correlation	Pearson correlation significance test	<0.0001	0.9696	0.94	N/A	N/A	N/A	C8: 7 mice, 19 sequences; L2: 8 mice, 13 sequences
1	D (C8. green)	Correlation	Pearson correlation significance test	<0.0001	0.9567	0.9158	N/A	N/A	N/A	
1	E (L2. orange)	Mean	Mean; Standard error of the mean	N/A	N/A	N/A	0.8175	0.05716	N/A	
1	E (C8. green)	Mean	Mean; Standard error of the mean	N/A	N/A	N/A	0.7468	0.05552	N/A	
1	F (L2. orange)	Mean	Mean; Standard error of the mean	N/A	N/A	N/A	N/A	N/A	N/A	
1	F (C8. green)	Mean	Mean; Standard error of the mean	N/A	N/A	N/A	N/A	N/A	N/A	
1	G (L2. orange)	Polar plot	Mean Vector; length of mean vector	N/A	N/A	N/A	354.288°	1.467°	0.936	
1	G (C8. green)	Polar plot	Mean Vector; length of mean vector	N/A	N/A	N/A	357.359°	2.213°	0.97	
1	G (L5. red)	Polar plot	Mean Vector; length of mean vector	N/A	N/A	N/A	198º	5.04	0.868	3 mice
S1	H (C8. green)	Correlation	Pearson correlation significance test	<0.0001	0.8187	0.6702	N/A	N/A	N/A	2 mice, 4 sequences
S1	H (le L5. orange)	Correlation	Pearson correlation significance test	<0.0001	0.7045	0.4964	N/A	N/A	N/A	
S1	H (ri L5. red)	Correlation	Pearson correlation significance test	<0.0001	0.7879	0.6208	N/A	N/A	N/A	
S1	I (le L5. orange)	Polar plot	Mean Vector; length of mean vector	N/A	N/A	N/A	357.97°	1.826°	0.971	
S1	I (ri C8. green)	Polar plot	Mean Vector; length of mean vector	N/A	N/A	N/A	1.432°	2.434°	0.949	
S1	I (ri L5. red)	Polar plot	Mean Vector; length of mean vector	N/A	N/A	N/A	185.835°	2.273°	0.954	
2	A, B, C, D	N/A	N/A	N/A	N/A	N/A	N/A	N/A	N/A	6 mice. control: 11 sequences; 0 Ca2+: 13 sequences; washout: 13 sequences
2	E, F, G	N/A	N/A	N/A	N/A	N/A	N/A	N/A	N/A	7 mice. control lumbar: 11 sequences; control cervical: 13 sequences; cervical after-cut: 9 sequences; lumbar after-cut: 6 sequences
2	H (orange dots)	Correlation	Pearson correlation significance test	0.0001	0.9983	0.9966	N/A	N/A	N/A	3 mice. control lumbar: 6 sequences; control cervical: 7 sequences; after-cut lumbar: 3 sequences; after-cut cervical: 3 sequences
2	H (grey circles)	Correlation	Pearson correlation significance test	0.0001	0.9817	0.9637	N/A	N/A	N/A	
2	I (control. ipsi.black)	Distribution of mean angle values	Mean Vector; length of mean vector	N/A	N/A	N/A	345.161	2.546	0.974	
2	I (control. contra. empty)	Distribution of mean angle values	Mean Vector; length of mean vector	N/A	N/A	N/A	162.803	4.285	0.943	
2	I (after cut. ipsi. orange)	Distribution of mean angle values	Mean Vector; length of mean vector	N/A	N/A	N/A	353.912	2.463	0.999	
2	I (after cut. contra. empty)	Distribution of mean angle values	Mean Vector; length of mean vector	N/A	N/A	N/A	177.873	4.909	0.939	
2	J (before cut)	Normal distribution	Paired t-test	0.1038	N/A	N/A	52.97	4.51	N/A	
2	J (after cut)	Normal distribution	Paired t-test	0.1038	N/A	N/A	66.49	5.96	N/A	
3	J	N/A	N/A	N/A	N/A	N/A	N/A	N/A	N/A	3 mice
4	D	Correlation	Pearson correlation significance test	0.031	-0.8699	0.75	N/A	N/A	N/A	1 mouse
4	E	Correlation	Pearson correlation significance test	0.47	0.7152	0.51	N/A	N/A	N/A	
4	F (light green. forelimb)	Correlation	Pearson correlation significance test	<0.0001	0.7248	0.5253	N/A	N/A	N/A	
4	F (dark green. hindlimb)	Correlation	Pearson correlation significance test	0.0852	0.3195	0.1021	N/A	N/A	N/A	
4	G	Polar plot	Mean Vector (μ); length of mean vector	N/A	N/A	N/A	18.272	8.61	0.718	
4	J	Correlation	Pearson correlation significance test	<0.0001	0.6569	0.4315	N/A	N/A	N/A	5 mice
4	J	Polar plot	Mean Vector (μ); length of mean vector	N/A	N/A	N/A	342.719	28.957	0.727	
4	K (left panel)	Correlation	Pearson correlation significance test	<0.0001	0.9873	0.9748	N/A	N/A	N/A	
4	K (right panel)	Polar plot	Mean Vector (μ); length of mean vector	N/A	N/A	N/A	355.641	7.53	0.991	
4	M (dark gray)	Correlation	Pearson correlation significance test	0.00366	0.9169	0.8395	N/A	N/A	N/A	
4	M (light gray)	Correlation	Pearson correlation significance test	<0.00001	0.5412	0.2929	N/A	N/A	N/A	

Supplementary Table 1. Statistical results and data samples. Related to Figure 1, 2, 3, 4 and Supplementary Figure 1.

Statistical table with data samples for each figure. SEM, standard error of the mean; N/A, non-applicable.

Supplemental Reference List

S1. Coulon, P., Derbin, C., Kucera, P., Lafay, F., Prehaud, C., and Flamand, A. (1989). Invasion of the peripheral nervous systems of adult mice by the CVS strain of rabies virus and its avirulent derivative AvO1. J Virol *63*, 3550–3554.

S2. Ugolini, G. (1995). Specificity of rabies virus as a transneuronal tracer of motor networks: transfer from hypoglossal motoneurons to connected second-order and higher order central nervous system cell groups. J. Comp. Neurol. *356*, 457–480.

S3. Ruigrok, T.J.H., Pijpers, A., Goedknegt-Sabel, E., and Coulon, P. (2008). Multiple cerebellar zones are involved in the control of individual muscles: a retrograde transneuronal tracing study with rabies virus in the rat. Eur J Neurosci *28*, 181–200.

S4. Morcuende, S., Delgado-Garcia, J.-M., and Ugolini, G. (2002). Neuronal premotor networks involved in eyelid responses: retrograde transneuronal tracing with rabies virus from the orbicularis oculi muscle in the rat. J Neurosci *22*, 8808–8818.